50. Resonances

Revised August 2023 by D.M. Asner (BNL), C. Hanhart (FZ Jülich) and M. Mikhasenko (Ruhr U. Bochum).

50.1 General Considerations

Perturbative methods can be applied to systems of quarks and gluons only for large momentum transfers (see review on 'Quantum Chromodynamics') and, under certain conditions, to some properties of systems that contain heavy quarks or very large momentum scales (see review on "Heavy-quark and soft-collinear effective theory"). Dealing with Quantum Chromodynamics (QCD) in the low momentum transfer region is a very complicated, non-perturbative problem. Most hadrons are resonances, which means that they appear as poles of the $\mathcal{S}$-matrix in the complex plane on unphysical sheets, a notion further detailed in Sec. 50.2. These resonances can show up either in so-called formation experiments,

$$A + B \to \mathbf{R} \to C_1 + ... + C_n \ ,$$

where they become visible in an energy scan (for example, the R-function measured in e^+e^- annihilation, *cf.* the corresponding plots in the review on "Plots of Cross Sections and Related Quantities"), or together with a spectator particle S in production experiments of the kind

$$A + B \to \mathbf{R} + S \to [C_1 + ... + C_n] + S \ ,$$
$$Z \to \mathbf{R} + S \to [C_1 + ... + C_n] + S \ ,$$

where the first reaction corresponds to an associated production, the second is a decay (see "Review of Multibody Charm Analyses"). In the latter case, the resonance properties are commonly extracted from a Dalitz-plot analysis (see review on "Kinematics") or projections thereof.

Resonance phenomena are very rich: while typical hadronic widths are of the order of $100\,\mathrm{MeV}$ (*e.g.*, for the meson resonances $\rho(770)$ or $\psi(4040)$ or the baryon resonance $\Delta(1232)$) corresponding to a lifetime of 10^{-23} s, the widths can also be as small as a few MeV (*e.g.* of $\phi(1020)$ or J/ψ) or as large as several hundred MeV (*e.g.* of the meson resonances $f_0(500)$ or $D_1(2430)$ or the baryon resonance $N(2190)$).

Typically, a resonance appears as a peak in the total cross section. If the structure is narrow and if there are no relevant thresholds or other resonances nearby, the resonance properties may be extracted employing a Breit–Wigner parameterization, if necessary improved by using an energy-dependent width (*cf.* Sec. 50.3.1 of this review). However, in general, unitarity and analyticity call for the use of more refined tools as outlined here as well as in recent review articles [1, 2]. When there are overlapping resonances with the same quantum numbers, the resonance terms should not simply be added but combined in a non-trivial way either in a $\mathcal{K}$-matrix approach (*cf.* Sec. 50.3.2 of this review) or using other advanced methods (*cf.* Sec. 50.3.5 of this review). Additional constraints from the $\mathcal{S}$-matrix allow one to build more reliable amplitudes and, in turn, to reduce the systematic uncertainties of the resonance parameters: pole locations and residues. In addition, for broad resonances there is no direct relation between pole location and the total width/lifetime — then, the pole residues need to be used in order to quantify the decay properties.

For simplicity, throughout this review the formulas are given for resonances in a system of distinguishable, scalar particles. The additional complications that appear in the presence of spins can be controlled in the helicity framework developed by Jacob and Wick [3], or in a non-covariant [4] or covariant [5] tensor-operator formalisms. Within these approaches, sequential (cascade) decays are commonly treated as a coherent sum of two-body interactions. Most of the expressions below are given for two-body kinematics.
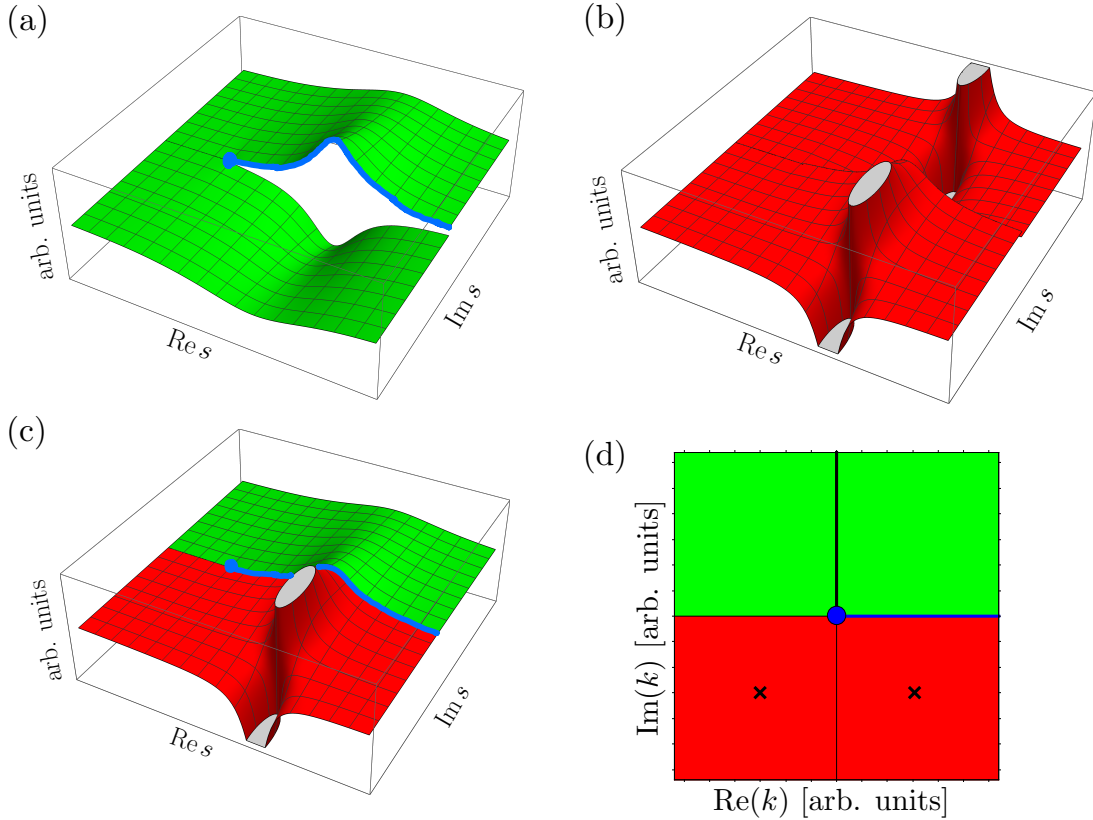
Figure 50.1: (a)-(c): Imaginary part of a typical scattering amplitude with an isolated resonance. The blue line shows the physical range of the Mandelstam variable s: it is real and starts from the threshold shown by the blue dot. Plot (a) shows the imaginary part of the amplitude in the complex s-plane that corresponds to the first or physical sheet (green surface), plot (b) shows the related unphysical or the second sheet (red surface) which contains the resonance poles, and plot (c) shows the analytic continuation of the same amplitude from the upper half plane of the physical sheet to the lower half plane of the unphysical sheet. The two sheets are connected smoothly along the real axis above the threshold. Panel (d) shows the k-plane, which is free of cuts. The upper (lower) half plane maps onto the physical (unphysical) sheet. Also here the blue line corresponds to the physically accessible values of the momentum k, which starts at threshold, where $k = 0$. The thick black line shows the analytic continuation of the on-shell momentum in the below threshold regime. The locations of the resonance poles are indicated by the black crosses.

50.1.1 *Properties of the $\mathcal{S}$-matrix*

The unitary operator that connects asymptotic *in* and *out* states is called the $\mathcal{S}$-matrix. The scattering amplitude is defined as the interacting part of the $\mathcal{S}$-matrix. For a two-particles scattering process, it reads:

$$i(2\pi)^4\delta^4(p_1 + p_2 - p_{1'} - p_{2'})\,\mathcal{M}(p_1, p_2; p_{1'}, p_{2'})_{ba}$$
$$= {}_{\text{out}}\langle p_{1'}p_{2'}, b|\,\mathcal{S} - 1\,|p_1 p_2, a\rangle_{\text{in}} \tag{50.1}$$

where $|p_1 p_2, a\rangle$ and $|p_{1'}p_{2'}, b\rangle$ are asymptotic states that can be treated as non-interacting particles in the spirit of the LSZ-reduction [6]. They carry the momenta p_1, p_2 and $p_{1'}$, $p_{2'}$, respectively.

The labels a and b are used to specify the *reaction channels.* In general terms, a reaction channel describes the possible outcome of a scattering event, characterized by the quantum numbers of the particles involved. Note, that in general $\mathcal{M}$ operates as a matrix in channel space, connecting the different asymptotic multi-particle states. For a single-particle state, we employ the relativistic normalization,

$$\langle p'|p\rangle = (2\pi)^3 2E_p\,\delta^3(\vec{p}\,' - \vec{p}), \tag{50.2}$$

with $E_p = \sqrt{\vec{p}\,^2 + m^2}$.

Mandelstam variables are defined as $s = (p_1 + p_2)^2$, $t = (p_1 - p_{1'})^2$, and $u = (p_1 - p_{2'})^2$. One finds that the the variables s, t, and u are not independent, since

$$s + t + u = m_1^2 + m_2^2 + m_{1'}^2 + m_{2'}^2$$

holds, where m_i with $i \in 1, 1', 2, 2'$ represents the masses of the involved particles. As a result, the reaction amplitude can be expressed as a function of two variables, $\mathcal{M}(s, t)$.

The Mandelstam variables play a crucial role in characterizing particle scattering. Specifically, the process described in Eq. (50.1) is known as *s-channel*, referring to a reaction, $1, 2 \to 1', 2'$. Here, $\sqrt{s}$ represents the total energy of the interacting system in the center-of-momentum frame. The variable t corresponds to the *momentum transfer*, which is related to the scattering angle, the angle between the momenta of particles 1 and $1'$ in the center-of-momentum frame (see also the review on "Kinematics" in this Review of Particle Physics). The scattering process with particles 1 and the antiparticle of $1'$, denoted by $\overline{1'}$, incoming to the antiparticle of 2, denoted by $\overline{2}$, and $2'$ outgoing represent a different reaction, it is referred to as the *t-channel* reaction. The scattering amplitudes of *s*- and *t*-channel are related via the so-called *crossing symmetry.* The *u-channel* is introduced analogously as a reaction with the initial state of particles 1 and $\overline{2'}$ and the final state of particles $1'$ and $\overline{2}$. The *t*-channel and the *u*-channel are referred to as the *crossed channels* relative to the reaction in Eq. (50.1). This relationship is illustrated in Fig. 50.2.
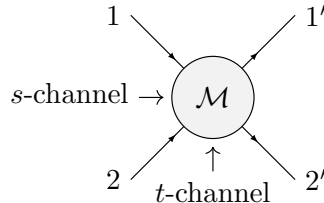

Figure 50.2: Illustration of the relation between *s*- and *t*-channel.

The analysis of resonance phenomena requires delving deeper into the complex analysis of the amplitude: $\mathcal{M}(s, t)$ is a multivalued function due to the complex *branch points* associated with the Mandelstam variables. These branch points emerge whenever a new channel becomes accessible, that is, whenever s exceeds $s_{\mathrm{thr},a} = (m_{1,a} + m_{2,a})^2$, where $m_{i,a}$ denotes the masses of the two particles in channel a. Every two-particle threshold introduces a square-root singularity. The square-root function is inherently double-valued; for instance, the equation $x = y^2$ has two solutions: $\sqrt{x}$ and $-\sqrt{x}$. In the complex plane, these two solutions are represented as separate layers or surfaces, known as *Riemann sheets* or Riemann surfaces. Consequently, each square-root singularity causes the number of Riemann sheets of the scattering amplitude to double. If a channel opens that has an odd number of particles, the branch point at the threshold exhibits a logarithmic singularity [7]. Such a branch point gives rise to an infinite number of sheets. The branch points come with their associated branch cuts — by convention those are taken from the threshold to infinity along the

real axis and accordingly called *right-hand cuts*. To explore a reaction amplitude in the complex energy plane, one can introduce a complex component to the Mandelstam variable s. The section of the complex plane that relates to a positive imaginary component of the relative momentum can be directly accessed from the physical region and is called the first Riemann sheet or the *physical sheet*. The other sheets are called *unphysical sheets*. The *physical axis* of an s-channel scattering amplitude represents a line for real values of the variable s larger than the lowest threshold to be evaluated on the physical sheet.

While the physical Riemann sheet is free of singularities off the real axis, the unphysical sheets may contain resonance poles and branch points. Branch points appear in the complex plane of an unphysical sheet when there is a resonance in a subsystem of involved particles [7,8]. The branch points related to thresholds in the crossed channels are located in the portion of the complex plane where the real part is negative and, therefore, are referred to as the *left-hand cuts*. An illustrative example for a left-hand cut is the one-pion exchange in nucleon-nucleon scattering that is located in the unphysical domain at $s = 4m_N^2 - m_\pi^2$. Triangle topologies, which are Feynman diagrams characterized by a triangular loop of three propagators, can lead to logarithmic singularities in the scattering amplitude. These singularities, appearing on the unphysical sheets, are often termed *triangle singularities* (TS) [7,9,10].

The reaction amplitude has poles that can be categorized as bound states, virtual states, or resonances. Poles corresponding to bound and virtual states manifest at real values of s. Specifically, *bound state* poles are found on the physical sheet, while *virtual state* poles are situated on an unphysical sheet, both being below the threshold. Resonance poles, on the other hand, emerge inside the complex plane of the unphysical sheets. Notably, those resonance poles that are on the unphysical sheet nearest to the physical region exert the most significant influence on experimental observables. Analyticity dictates that for every pole at a specific complex value of s_p, there must be a corresponding pole at its complex conjugate value s_p^*. This relationship is a direct consequence of the *Schwarz reflection principle*, a mathematical technique utilized for analytic continuation within scattering theory. For a single-channel case, the complex structure of an amplitude with a single resonance is illustrated in Fig. 50.1(a)-(c). Among the two poles, symmetrically positioned relative to the real axis on the second sheet, the one exhibiting a negative imaginary part seamlessly connects to the physical axis, which becomes especially clear in panel (c) of the figure where the physical axis is shown as the blue line. It therefore has a more pronounced effect on observables in the vicinity of the resonance region compared to its conjugate counterpart. The shortest continuous path from the physical region to the second sheet pole with the positive imaginary part is via a line that goes around the threshold. However, as the extra path around the threshold diminishes in the near-threshold region, the effective distance to both poles becomes comparable for near threshold kinematics, thereby rendering the influence of both poles on observables similarly significant.

An alternative way to depict the complex structure is through the k-plane, where k denotes the relative momentum of the two scattering particles in their center-of-momentum frame. For particles of equal mass, denoted as m (expression for unequal masses is given in Eq. (50.7)), one finds

$$k = \frac{1}{2}\sqrt{s - 4m}\,. \tag{50.3}$$

Unlike the complex s-plane, the k-plane does not have a two-body threshold cut. Consequently, both the physical and unphysical Riemann sheets, which are linked to the branch point in s are mapped onto the upper and lower half of the complex k-plane, respectively. The k-plane is sketched in Fig. 50.1(d), including possible locations of resonance poles. In this representation it becomes especially clear that only one resonance pole drives the dynamics on the physical axis in the resonance region, while at the threshold, where $k = 0$, both poles are of equal significance.

In situations involving two relevant channels, we encounter four Riemann sheets. These are illustrated in the left panel of Fig. 50.3. For a non-relativistic system with two channels, this four-sheeted Riemann surface can be transformed into a plane represented by a new variable, ω. This variable is defined in relation to the channel-momenta, as detailed in references [11,12] (for a recent application see Ref. [13])

$$k_1 = \sqrt{\frac{\mu_1 \Delta}{2}} \left(\omega + \frac{1}{\omega} \right) , \quad k_2 = \sqrt{\frac{\mu_2 \Delta}{2}} \left(\omega - \frac{1}{\omega} \right) , \qquad (50.4)$$

where Δ denotes the energy difference between the two thresholds and the μ_a the reduced mass of the particles in channel a, $\mu_a = m_{1,a} m_{2,a}/(m_{1,a} + m_{2,a})$. The lower threshold is located at $\omega = i$, the higher at $\omega = 1$. The mapping of the Riemann sheets and the different areas in the ω-plane is shown in the right panel of Fig. 50.3. The ω-plane nicely shows how the different sheets connect to each other.[1] The solid green line shows the physical axis in the physical regime. The thick black line its analytic continuation below the lowest threshold. The pronounced kinks in this line for the ω plane show the thresholds. Please observe that for $\omega \approx i$ the sheet structure agrees to panel (*d*) of Fig. 50.1, since in this kinematic regime the second channel does not matter.

In the context of a two-channel scenario, the proximity of a sheet to the physical axis varies with increasing energy. Specifically, for energies that exceed the first threshold, but remain below the second, sheet (21) is the one that smoothly connects to the upper half-plane of the physical sheet (11). Once the energy surpasses the second threshold, sheet (22) assumes this role. As a result, any pole on sheet (21) that lies above the second threshold will manifest in the data solely as a cusp right at the second threshold. Sheet (12), on the other hand, is remote for almost all energies.

Singularities, poles and branch points determine the visible structures in observables. However, it is crucial to note that not every observable bump is indicative of a resonance as discussed in [14]. Under certain kinematic conditions, Triangle Singularities, in particular, can either mimic resonance signals, as suggested in Refs. [15–20], or significantly alter resonance signals [21]. Conversely, not all resonances produce a noticeable bump across all observables. For example, in the baryon sector, there is no clear trace of the $N(1440)1/2^+$, the so called Roper resonance, in the πN observables or phase shifts, although careful analyses reveal a pole [22]. In the meson sector, the $f_0(500)$, also known as σ meson, was firmly established only after the application of very sophisticated theoretical analysis tools (see, *e.g.*, Ref. [23] for a review). This complexity arises because the scalar-isoscalar $\pi\pi$ phase shifts reach 90 degrees near 800 MeV, which is approximately 400 MeV above the resonance mass. At this energy, the onset of the next resonance, the $f_0(980)$, is already observable. The analyticity principle of the $\mathcal{S}$-matrix germane to quantum scattering theories, dictates that only poles and branch points can exist on the real axis of the first Riemann sheet, excluding any singularities in the complex plane. This principle is closely linked to causality, ensuring that effects follow their causes in a chronological order. In non-relativistic scattering, the analyticity finds a solid mathematical base [24]. Similarly, perturbative relativistic theory maintains this analyticity through a series expansion of the $\mathcal{S}$-matrix, each term depicted by a Feynman diagram, representing processes with distinct analytical expressions. A deeper level of analyticity is proposed by the Mandelstam hypothesis, suggesting not only the analytic properties of the scattering amplitude within the complex plane of the first Riemann sheet but also a nuanced interconnection between crossed scattering processes through analytic continuation [25].

Unitarity further constrains the imaginary part of the amplitude on this real axis, a topic we will explore in the subsequent section. Additional constraints are introduced by principles such as

---

[1]An alternative illustration for this two-channel case as well as an extension to three channels can be found in Ref. [2].
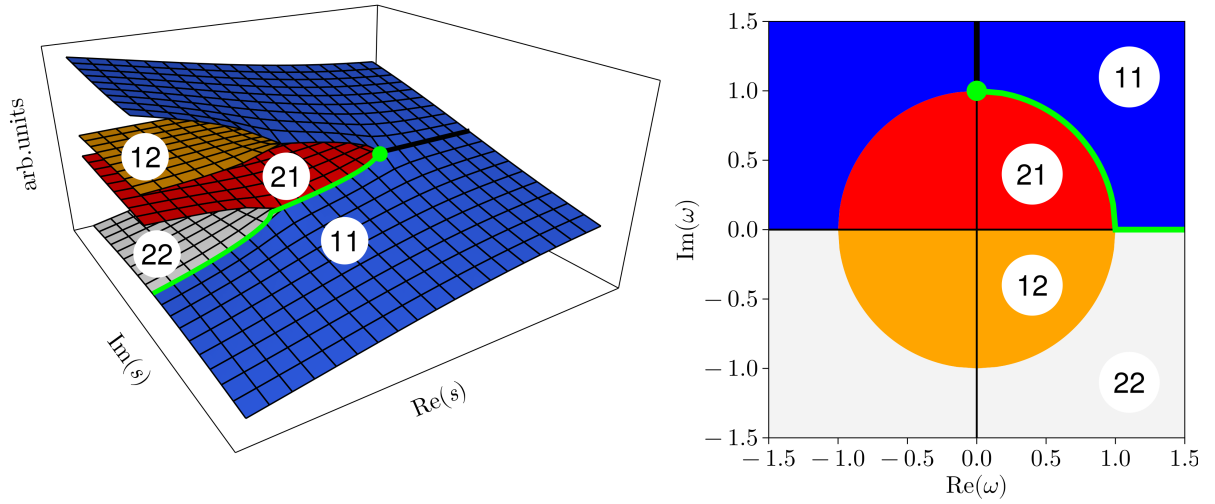
Figure 50.3: Cut structure of the $\mathcal{S}$-matrix with two channels present. The diagrams feature four sheets, labeled (ij), where both i and j can be 1 or 2. These labels indicate the doubling of the sheets at the first and second thresholds. The left panel displays the complex s plane, while the right panel represents the ω plane. The physical axis, along with its analytic continuation below the threshold, is highlighted with a thick solid line, green in the physical regime, black for the analytic continuation below the lowest threshold.

crossing symmetry, duality [26] and positivity [27]. Approaches based on analyticity and crossing symmetry have been implemented through dispersion theory. Among the most notable are the Roy equations and their variants [28]. These have been applied to a range of processes, including $\pi\pi \to \pi\pi$ [29–31], πK scattering [32], $\gamma\gamma \to \pi\pi$ interactions [33], and pion-nucleon scattering [34,35].

50.1.2 *Consequences from unitarity*

Scattering amplitudes, denoted as $\mathcal{M}$, and production amplitudes, represented by $\mathcal{A}$, have distinct characteristics due to the different constraints imposed by unitarity. When considering the scattering amplitude, it is assumed that all channels hold similar significance. In contrast, for production amplitudes, it is assumed that for the dynamics of the particles in the final state the initial state does not play a role. Accordingly, the interactions in the final state among the produced particles are described by relevant scattering amplitudes of those particles only. Scattering processes are for example $\pi^+\pi^- \to K\bar{K}$ and $D^0\bar{D}^0 \to D^0\bar{D}^0$. Examples for production processes are $e^+e^- \to \gamma^* \to \pi^+\pi^-$, which provides access to the pion vector form factor, $\tau^- \to K^-\pi^0\nu_\tau$, and $B^0 \to J/\psi\pi^+\pi^-$.

The unitarity of the $\mathcal{S}$-matrix, represented by the equation $S^\dagger S = 1$, ensures the conservation of probability. This principle imposes a specific constraint on the imaginary part of the reaction amplitude. Below the lowest threshold, the amplitude remains real. However, once the energy is higher than the threshold, there is a discontinuity associated with the threshold branch point. The $\mathcal{S}$-matrix unitarity relates the value of the discontinuity, to the amplitude itself [6]:

$$\text{Disc}\,\mathcal{M}_{ba} = \mathcal{M}_{ba} - \mathcal{M}_{ab}^* = i\,(2\pi)^4 \sum_c \int d\Phi_c \mathcal{M}_{cb}^* \mathcal{M}_{ca}\ , \tag{50.5}$$
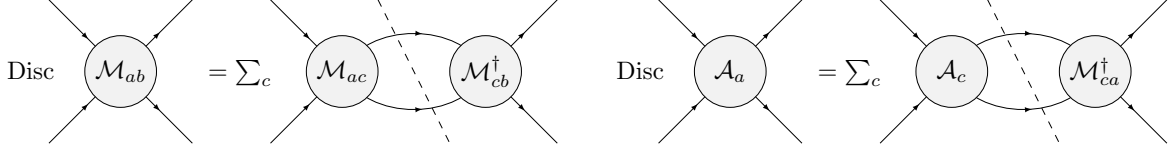
Figure 50.4: Graphical illustration of the discontinuity equations for the scattering and the production amplitude, respectively. The dashed line indicates that the intermediate state is to be put on-shell to find the discontinuity.

where $d\Phi_c$ denotes the invariant phase space for a given channel, labeled as c. The factor $(2\pi)^4$ aligns with the definition of the phase space expression (see Eq. (12) in the review on "Kinematics"). It is essential to note that the summation only considers open channels, meaning those with a production threshold below the scattered system's energy. In the evaluation of an actual Feynman diagram the discontinuity can be extracted by employing the Cutkosky rule, which comprises replacing the propagators in the pertinent intermediate state by delta-distributions. Eq. (50.5) is illustrated graphically in Fig. 50.4. The left part of the expression yields $2i\,\mathrm{Im}\mathcal{M}_{ba}$ in accordance to analytic properties of reaction amplitude [36]. For the forward scattering, $t = 0$, the right part of Eq. (50.5) resembles the total cross section up to a kinematic factor, a relationship know an the optical theorem:

$$\mathrm{Im}\,\mathcal{M}_{aa}(s,0) = 2q_a\sqrt{s}\,\sigma_{\mathrm{tot}}(a \to \mathrm{anything})\,. \tag{50.6}$$

In this equation, q_a represents the break-up momentum of the particles in the center-of-momentum frame,

$$q_a = \frac{\lambda^{1/2}(s, m_{1,a}^2, m_{2,a}^2)}{2\sqrt{s}}\,, \tag{50.7}$$

where $\lambda(x, y, z) = x^2 + y^2 + z^2 - 2xy - 2yz - 2xz$ is the Källén function, and the masses of the two particles in the channel a, $m_{1,a}$ and $m_{2,b}$, *cf.* Eq. (17) of the review on "Kinematics".

The unitarity relation for a production amplitude in channel a is represented by:

$$\mathrm{Disc}\,\mathcal{A}_a = \mathcal{A}_a - \mathcal{A}_a^* = i\,(2\pi)^4 \sum_c \int d\Phi_c \mathcal{M}_{ca}^* \mathcal{A}_c\,. \tag{50.8}$$

Equation (50.8) is illustrated graphically in Fig. 50.4. A direct consequence of this equation is that the production amplitude shares its poles with the scattering amplitude. A common method to model the production amplitude that adheres to this unitary relation is to express it as a linear combination of the scattering amplitudes. This approach, known as the $\mathcal{Q}$-vector method (see Sec 50.3.4), has its limitations. Specifically, production amplitude inherits the left-hand singularities of the scattering amplitude, while, in general, it has a different cut structure. To address this drawback, a more sophisticated method, known as *unitarization* is employed. This method, rooted in dispersion theory, offers a more refined approach to the problem and is detailed in [37]. A notable application of this method is the Khuri-Treiman framework [38, 39], which is frequently used to study three-body decays. This framework has been successfully applied to a range of decays, from light mesons [40–52] to heavy-flavour decays [53–55].

50.1.3 *Partial-wave decomposition*

It is often convenient to expand a two-body scattering amplitude of a two-body subsystem of a production amplitude in partial waves. Since resonances have a well-defined spin, they appear
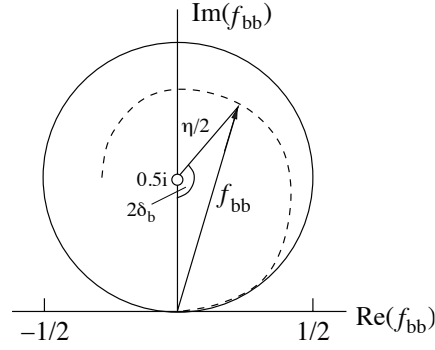
Figure 50.5: Argand plot showing a trajectory of the diagonal element of a partial-wave amplitude, f_{bb}, as a function of energy in the complex plane. As the energy increases the amplitude follows the line counter clockwise. The amplitude leaves the unitary circle (solid line) as soon as inelasticity sets in, $\eta < 1$ (dashed line).

only in a specific partial wave of the reaction amplitude. For scalar particles, the expansion reads:

$$\mathcal{M}_{ba}(s,t) = \sum_{j=0}^{\infty} (2j+1)\mathcal{M}_{ba}^{j}(s)P_{j}(\cos(\theta)) , \qquad (50.9)$$

where j denotes the total angular momentum and the $P_{j}(\cos(\theta))$ denotes the Legendre polynomials. In the presence of spins an expansion more complicated than Eq. (50.9) is necessary — for a general discussion on how to handle spins see *e.g.* Ref. [56]. In the absence of spins the parameter j coincides with the orbital angular momentum of the particle pairs in the initial and the final state. To simplify notation and since all amplitudes from here on are understood to be partial wave projected, we drop the label j for the single-argument function $\mathcal{M}_{ba}(s)$. Plugging Eq. (50.9) into Eq. (50.5) one finds the unitarity relation for the partial-wave amplitude $\mathcal{M}_{ba}(s)$, namely

$$\mathrm{Im}\,\mathcal{M}_{ba}(s) = \sum_{c} \mathcal{M}_{cb}(s)^{*}\,\rho_{c}(s)\,\mathcal{M}_{ca}(s) \qquad (50.10)$$

with $\rho_{c}(s)$ being a factor that is related to the two-body phase space in Eq. (12) of the review on "Kinematics",

$$\rho_{c}(s) = \frac{(2\pi)^{4}}{2} \int \mathrm{d}\Phi_{2} = \frac{1}{16\pi} \frac{2|\vec{q}_{c}|}{\sqrt{s}} , \qquad (50.11)$$

with the momentum q_{c} being defined in Eq. (50.7). Note that in case of the two particles being identical the inclusion of symmetry factors becomes necessary. The partial-wave amplitude $f_{ba}(s)$ is introduced by normalizing scattering amplitude with the phase spaces factors,

$$f_{ba}(s) = \sqrt{\rho_{b}}\,\mathcal{M}_{ba}(s)\,\sqrt{\rho_{a}}. \qquad (50.12)$$

The unitarity condition for f_{ba} follows from Eq. (50.10):

$$\mathrm{Im}\,f_{ba}(s) = \sum_{c} f_{cb}^{*}(s)f_{ca}(s). \qquad (50.13)$$

It leads us to deduce that the inverse of the imaginary part of f_{ba} is equal to $-\delta_{ba}$. Moreover, $\mathcal{S} = \mathbb{I} + 2if$ is a unitary matrix. Hence, the diagonal elements of f can be parameterized as

$$f_{bb} = (\eta_{b}\exp(2i\delta_{b}) - 1)/2i , \qquad (50.14)$$

where δ_b denotes the phase shift for the scattering from channel b to channel b and η_b is the elasticity parameter, also known as inelasticity. Building upon Eq. (50.13), we can further deduce that,

$$\text{Im } f_{bb}(s) = (1 - \eta_b \cos(2\delta_b))/2 = \sum_c |f_{cb}(s)|^2 \ . \tag{50.15}$$

Using Eq. (50.14) for the last term in the sum, we obtain a relation highlighting the meaning of the inelasticity,

$$\frac{1}{4}(1 - \eta_b^2) = \sum_{c \neq b} |f_{cb}(s)|^2 \ . \tag{50.16}$$

It is important to note that the parameter η_b is confined within the range $[0, 1]$, where the case, $\eta_b = 1$ is referred to as a purely elastic scattering. Thus, the function $\eta_b(s)$ is a direct measure of the contribution of the inelastic channels on the scattering amplitude in a given channel.

The evolution of the partial-wave amplitude f_{bb} with energy can be displayed as a trajectory in the Argand plot, as shown in Fig. 50.5. In case of a two-channel problem, $\eta_1 = \eta_2 = \eta$, and the off-diagonal element is $f_{12} = \sqrt{1 - \eta^2}/2 \exp(i(\delta_1 + \delta_2))$. The unitarity condition Eq. (50.14) sets the limit to the squared amplitude f_{bb}:

$$|f_{bb}|^2 = \frac{1}{4}(\eta_b^2 - 2\eta_b \cos(2\delta_b) + 1) \leq \frac{1}{4}(\eta_b + 1)^2 \ , \tag{50.17}$$

where the maximum value is reached for $\delta_b = \pi/2$. For the absolute square of the partial-wave-projected scattering amplitude the unitarity bound thus reads:

$$|\mathcal{M}_{bb}| \ \leq \ \frac{1}{2\rho_b}(\eta_b + 1) \ \leq \ \frac{8\pi}{q_b}\sqrt{s} \,, \tag{50.18}$$

where the second inequality comes from $\eta_b \leq 1$. For energies much larger than the masses of the scattering particles the upper bound for $|\mathcal{M}_{bb}|$ tends to 16π for large s.

The partial-wave projected production amplitude $\mathcal{A}(s)$ (note that the label j has been omitted for consistency) is also constrained by unitarity. As derived from Eq. (50.8):

$$\text{Im } \mathcal{A}_a = \sum_b \mathcal{M}_{ba}^* \rho_b \mathcal{A}_b \ , \tag{50.19}$$

where the summation encompasses all open channels. In the realm of elastic scattering, solely one channel, denoted by a, contributes to the sum. Consequently, the phase of $\mathcal{A}_a$ must align with the phase of $\mathcal{M}_{aa}$, given that the left-hand side of Eq. (50.19) represents a real value. This principle is recognized as the *Watson theorem* [57]. To illustrate, consider the phase of the pion vector form factor: it agrees to that of $\pi\pi$ scattering in the vector isovector channel (aside from effects of the isospin-violating $\rho - \omega$ mixing) up to about $1\,\text{GeV}$, where inelastic contributions start gaining significance.

50.2 Properties of resonances

A resonance is defined by its *pole position* in the complex s-plane, denoted as s_R, and by the strength parameters of its couplings to various decay channels evaluated at this pole, known as the *pole residues*. The pole mass M_R and pole width Γ_R are defined via the pole parameters

$$\sqrt{s_\text{R}} = M_\text{R} - i\Gamma_\text{R}/2 \ . \tag{50.20}$$

For states where the relevant thresholds are situated significantly below the resonance location, the lifetime τ_R of the resonance is given by $\tau_\text{R} = 1/\Gamma_\text{R}$ (refer to the review on "Kinematics" and

for a recent discussion, see Ref. [58]). It is important to note that the conventional Breit–Wigner parameters $M_{\rm BW}$ and $\Gamma_{\rm BW}$, introduced in Eq. (50.30), differ from the pole parameters due to finite width effects and the influence of thresholds and background terms. It should be stressed that pole location $s_{\rm R}$ and pole residues are the only resonance properties that are model and parameterization independent.

When a resonance interacts with multiple channels, each channel contributes to the imaginary part of the pole position. However, these individual imaginary contributions do not necessarily simply sum up, leading to the need for redefining the partial widths. This behavior is discussed on the example of the $f_0(980)$ in Refs. [59,60].

In the close vicinity of the resonance pole one defines the residues via

$$\lim_{s \to s_{\rm R}} (s - s_{\rm R})\mathcal{M}_{ba} = -\mathcal{R}_{ba} \ . \tag{50.21}$$

Those can be conveniently calculated via an integration along a closed contour around the pole using

$$\mathcal{R}_{ba} = -\frac{1}{2\pi i} \oint ds \mathcal{M}_{ba} \ . \tag{50.22}$$

The residue adheres to the factorization relation, $(\mathcal{R}_{ba})^2 = \mathcal{R}_{aa} \times \mathcal{R}_{bb}$. This factorization emerges as a universal property stemming from the unitarity of scattering processes [7]. Building on this relation, one can define *pole couplings* as follows:

$$\tilde{g}_a = \mathcal{R}_{ba}/\sqrt{\mathcal{R}_{bb}} \ . \tag{50.23}$$

The pole couplings characterize the transition strength of a given resonance to some channel a independently of how the particular resonance was produced. They are in general complex valued.

In the baryon sector, it is customary to define the residue of the pole for the f_{ba} amplitude (as described in Eq. (50.13)) in terms of the variable $\sqrt{s}$ rather than s. This residue can be related to the residues mentioned earlier by:

$$r_{ba} = \frac{1}{2}\sqrt{\frac{\rho_a(s_{\rm R})\rho_b(s_{\rm R})}{s_{\rm R}}} \, \mathcal{R}_{ba} \ , \tag{50.24}$$

where the phase-space factors are to be continued analytically to the pole location $s_{\rm R}$. The residues quoted in the baryon listings are those for πN scattering ($a = b = \pi N$).

The branching ratio of a resonance decay to a specific channel represents the fraction of the decay probability directed to that channel.

$$\mathrm{Br}_a = N_a/N_{\rm tot} \ . \tag{50.25}$$

Here, N_a is the experimental count of events for the decay channel $R \to a$, while $N_{\rm tot}$ represents the total number of events produced in the decay of the resonance. Since the amplitudes of decays to different final states add incoherently, we have $N_{\rm tot} = \sum_b N_b$. We note, however, that both N_a and $N_{\rm tot}$ may exhibit a dependence on the reaction through which the resonance is produced, due to the resonance's finite width. For a narrow resonance, the experimental count is determined by integrating the squared production amplitude over the decay channel's phase space:

$$N_a = N_0 \int |\mathcal{A}_a|^2 \, \mathrm{d}\Phi_a \ , \tag{50.26}$$

where N_0 is a normalization constant associated with the integrated luminosity, and $\mathcal{A}_a$ represents the amplitude of the resonance decay to channel a. When the decay rate's variation across the resonance width becomes significant, the resonance's lineshape must be considered:

$$N_a = N_0 \int_{s_{\text{thr},a}}^{\infty} \mathrm{d}s \sigma_{\text{R}}(s) \int |\mathcal{A}_a(s)|^2 \, \mathrm{d}\Phi_a(s) \ . \tag{50.27}$$

Here, $\sigma_{\text{R}}(s)$ denotes a proper weight function of the resonance and $s_{\text{thr},a}$ is the threshold value for the channel a. Additionally, the phase space integral, $\Phi_a(s)$, puts the integrand to zero below the energy threshold of the decay channel a. This aspect is particularly crucial for the decays of broad resonances into channels with energy thresholds exceeding the resonance's nominal mass. This methodology is frequently employed in light-meson studies, as demonstrated in Ref. [61], and is also prevalent in light baryon research, as referenced in Ref. [60].

In case of the decay of some heavy state into multi-body final states, the transition amplitude can include resonances within subsystems of particles. When the total amplitude is decomposed as $\mathcal{A}_a = \sum_{\text{R}} \mathcal{A}_{a(\text{R})}$, the relative branching fraction for the decay of the given heavy state into final state a via resonance R in some subsystem, denoted as $\text{Br}_{a(\text{R})} / \text{Br}_a$, is given by:

$$\text{Br}_{a(\text{R})} / \text{Br}_a = \int \left| \mathcal{A}_{a(\text{R})} \right|^2 \mathrm{d}\Phi_a \bigg/ \int |\mathcal{A}_a|^2 \, \mathrm{d}\Phi_a \tag{50.28}$$

It is crucial to recognize that the decomposition of the total amplitude, $\mathcal{A}_a$, into resonance amplitudes, $\mathcal{A}_{a(R)}$, is not a straightforward process. Beyond the differentiation of components based on distinct quantum numbers, this separation is inherently model-dependent. Furthermore, it is essential to be aware that the amplitudes $\mathcal{A}_{a(R)}$ can interfere with one another. As a result, their individual probabilities might not sum up to the total branching fraction of channel a. Nonetheless, in many scenarios, the interference contributions are small, making the fractions $\text{Br}_{a(\text{R})} / \text{Br}_a$ indicative. For recent applications of these formulas in the context of B-decays see Refs. [62–65].

Lastly, an expression analogous to the branching fraction can be formulated using the pole parameters. For two-particle decays in the S-wave, one writes:

$$\text{Br}_a = \frac{|\tilde{g}_a|^2}{M_{\text{R}} \Gamma_{\text{R}}} \rho_a(M_{\text{R}}^2) \ , \tag{50.29}$$

where M_{R} and Γ_{R} have been previously defined in Eq. (50.20). This approach was utilized to define a two-photon width for the broad $f_0(500)$ resonance [66, 67]. Similarly, one should use residues to quantify the coupling of resonances to certain production channels [68]. For an application of this approach to the coupling of the $K_0^*(1430)$ resonance to a leptonic current see Ref. [69]. Equation (50.29) provides a definition of branching fraction that remains independent of the reaction used to derive the quantity. For narrow resonances, this definition aligns well with Eq. (50.25) and Eq. (50.26). However, for broad, overlapping resonances, it is essential to recognize that Eq. (50.29) is primarily used to convert residues into metrics that facilitate a more straightforward comparison of resonance transitions across different channels. For resonances with a coupling to a channel that remains closed at the resonance mass, Eq. (50.29) is not applicable due to the phase-space factor. In such scenarios, modification of the expression is required as elaborated upon in Ref. [60], and at the conclusion of Sec. 50.3.5.

50.3 Common parameterizations

In general, there is no universal, model-independent recipe to build scattering amplitudes. However, a few approaches presented in this section are practical to extract resonance properties

in experimental analyses. The systematic theory uncertainties need to be assessed from a range of model variations that provide a sufficient quality of description of the available data and are permitted by general $\mathcal{S}$-matrix principles and the symmetries controlling the system at hand.

50.3.1 *The Breit–Wigner parameterization*

The relativistic Breit–Wigner parameterization represents a dressed propagator for an isolated resonance. The production amplitude for a resonance observed in a channel a, is given by

$$\mathcal{A}_a(s) = \frac{\mathcal{N}_a(s)}{M_{\mathrm{BW}}^2 - s - iM_{\mathrm{BW}}\Gamma(s)} \tag{50.30}$$

where M_{BW} represents the Breit–Wigner mass, and $\Gamma_{\mathrm{BW}} = \Gamma(M_{\mathrm{BW}}^2)$ denotes the Breit–Wigner width. The function $\Gamma(s)$ is defined by the channels to which the resonance can decay. The numerator function $\mathcal{N}_a(s)$ is tailored to the production process, encompassing kinematic factors and couplings pertinent to both the production and decay processes.

$$\mathcal{N}_a(s) = \alpha\, g_a\, n_a(s) \tag{50.31}$$

$$\Gamma(s) = \frac{1}{M_{\mathrm{BW}}} \sum_b g_b^2 \rho_b(s) n_b^2(s) \,, \tag{50.32}$$

Here the index $b = 1, 2, \ldots$ runs over all decay channels of the resonance. The coupling constants are represented by g_b, and ρ_b is the phase-space factor as defined in Eq. (50.11). The expression for $n_a(s)$ is:

$$n_a = (q_a/q_0)^{l_a} F_{l_a}(q_a/q_0)\,, \tag{50.33}$$

where l_a indicates the orbital angular momentum in channel a, $q_a(s)$ is the break-up momentum as defined in Eq. (50.7), and q_0 is a suitably selected momentum scale. The term $(q_a)^{l_a}$ ensures the amplitude's appropriate threshold behavior. The rapid growth of this factor for angular momenta $l_a > 0$ is offset at specific s values by a phenomenological form factor, represented here by $F_{l_a}(q_a, q_0)$ — the presence of these suppression factors is also a requirement from positivity which demands that the dressed propagator, the denominator of Eq. (50.30) and similar equations below, is not allowed to drop faster than $1/s$ [27]. The Blatt-Weisskopf form factors are frequently employed in the literature [70–72] to model F_j:

$$F_0^2(z) = 1\,, \tag{50.34}$$
$$F_1^2(z) = 1/(1 + z^2)\,,$$
$$F_2^2(z) = 1/(9 + 3z^2 + z^4)\,,$$

where $z = q/q_0$, the scale parameter $1/q_0$ typically falls within the range of $1\,\mathrm{GeV}^{-1}$ to $5\,\mathrm{GeV}^{-1}$. Rather than employing coupling constants as in Eq. (50.32), channel partial widths can be used,

$$\Gamma(s) = \sum_b \Gamma_{\mathrm{BW},b} \frac{\rho_b(s)}{\rho_b(M_{\mathrm{BW}}^2)} \left(\frac{q_b}{q_{b\,\mathrm{R}}}\right)^{2l_b} \frac{F_{l_b}^2(q_b, q_0)}{F_{l_b}^2(q_{b\,\mathrm{R}}, q_0)}\,. \tag{50.35}$$

Here $q_{b\,\mathrm{R}}$ is the values of the break-up momenta evaluated at $s = M_{\mathrm{BW}}^2$. It is essential to note that this substitution is valid only for channels where the decay channel's threshold is positioned below the nominal resonance mass. In other scenarios, Eq. (50.32) should be applied.

Equation (50.32) incorporates a threshold for each of the coupled channels. The expression is straightforward to use in the physical region above all the thresholds. Its evaluation elsewhere requires a careful analytic continuation. As outlined in Refs. [73, 74], the choice

$$q_c = i\sqrt{-q_c^2} \quad \text{for} \quad q_c^2 < 0\,, \tag{50.36}$$

leads to an evaluation of the amplitude on the physical sheet below threshold. The *Flatté parameterization* [73] refers to the two S-wave channels' amplitude near a threshold of a heavier channel in the physical region of the lighter channel computed with Eq. (50.36). When a resonance's coupling to the channel with a higher threshold is notably strong, the parameterization displays scaling invariance. This implies that it is not possible to extract individual partial decay widths; only their ratios can be determined [75].

The Breit–Wigner parameterization is an accurate representation of resonance phenomena strictly in the $\Gamma/\Delta \to 0$ limit, where Γ is the resonance width and Δ is the distance to the closest unaccounted singularity, be it a pole of a higher resonance or a kinematic threshold related to a coupled channel. However, the situation is often more complex due to multiple singularities in the complex plane around the resonance with different importance. For instance, in P-wave $\pi\pi$ scattering, the Breit–Wigner parameterization aptly describes the ρ-meson resonance over an extensive range. Although the closest singularity to the ρ-meson pole is the ω-pole ($\Gamma_\rho/\Delta_\omega \gg 1$), this isospin breaking effect is typically insignificant except few special cases [76, 77]. Subsequent singularities, namely the 3π, 4π, and 6π thresholds, are also generally disregarded. The two-pion threshold is incorporated in the Breit-Wigner parameterization through an energy-dependent width. Finally, the parameterization's efficacy diminishes around $1.2\,\mathrm{GeV}$ due to the ρ' resonance, situated approximately at 1.45 GeV.

Once the applicability of the Breit-Wigner parameterization is established, it is crucial to recognize that its parameters will only align with the pole parameters if the width is small. Yet, extracting the pole position from the Breit-Wigner amplitude is a straightforward technical task, achieved through analytic continuation. However, neither the Breit–Wigner parameters nor the corresponding pole parameters should be deemed reliable without justifying the parameterization's applicability. If there is more than one resonance in one partial wave that significantly couples to the same channel, it is generally inappropriate to employ a sum of Breit–Wigner functions. Such an approach often results in a breach of unitarity constraints, potentially introducing an indeterminate bias to the inferred resonance properties from the reaction amplitude. For overlapping resonances in the same partial wave, more sophisticated methods, such as the $\mathcal{K}$-matrix approach detailed in the subsequent section, are recommended.

50.3.2 $\mathcal{K}$-*matrix approach*

The $\mathcal{K}$-*matrix* method offers a comprehensive framework for modelling coupled-channel amplitudes [78]. This method ensures two-particle unitarity. However, it traditionally omits the left-hand cuts. The scattering amplitude $\mathcal{M}_{ba}(s)$ can be derived from the equation:

$$n_b \, \mathcal{M}_{ba}^{-1} \, n_a = \mathcal{K}_{ba}^{-1} - i\delta_{ba}\rho_a n_a^2 \,. \tag{50.37}$$

Here, $\mathcal{K}_{ba}$ represents a real function and is subject to modeling. The factor n_a is elaborated upon in Eq. (50.33). Since there is no unique recipe to build $\mathcal{K}$, it is essential to explore various parameterizations to gauge the theoretical systematic uncertainty. A commonly adopted choice for the $\mathcal{K}$-matrix is given by:

$$\mathcal{K}_{ba}(s) = \sum_{\mathrm{R}} \frac{g_b^{\mathrm{R}} g_a^{\mathrm{R}}}{m_{\mathrm{R}}^2 - s} + b_{ba} \,, \tag{50.38}$$

where m_{R} is referred to as the bare mass of the resonance R (not to be confused with the physical mass), and the g_a^{R} represents the bare couplings of the resonance R to the channel a (not to be confused with the residues). The b_{ba} is a matrix that parameterizes the non-pole components of the $\mathcal{K}$-matrix. Provided all parameters in Eq. (50.38) are real, the amplitude $\mathcal{M}_{ba}(s)$ remains unitary. From Eq. (50.37), the scattering amplitude $\mathcal{M}$ can be directly computed using its matrix form:

$$\mathcal{M} = n[1 - \mathcal{K} \, i\rho \, n^2]^{-1} \mathcal{K} \, n \,, \tag{50.39}$$

where n and ρ are diagonal matrices, $n = \mathrm{diag}(n_a, n_b, \dots)$, and $\rho = \mathrm{diag}(\rho_a, \rho_b, \dots)$. As an alternative to Eq. (50.38), the same functional structure on the right side of Eq. (50.38) can be employed to parameterize the inverse $\mathcal{K}$-matrix, termed the M-matrix, by the authors of Ref. [79]. Numerous alternative formulations within the $\mathcal{K}$-matrix framework are utilized for amplitude studies related to lattice-QCD calculations [80–82].

A prevalent method to construct the production amplitude within the $\mathcal{K}$-matrix framework is the $\mathcal{P}$-*vector* parameterization [72, 78, 83]. The method utilizes the $\mathcal{K}$-matrix poles and bare couplings from Eq. (50.38):

$$\mathcal{A}_a(s) = n_a \sum_c \left[1 - \mathcal{K} \, i\rho n^2 \right]^{-1}_{ac} \mathcal{P}_c \,, \tag{50.40}$$

$$\mathcal{P}_c = \sum_{\mathrm{R}} \frac{\alpha^{\mathrm{R}} g_c^{\mathrm{R}}}{m_{\mathrm{R}}^2 - s} + \mathcal{B}_c. \tag{50.41}$$

The production vector, denoted as $\mathcal{P}_c$, comprises two main components. The first component represents a transition driven by the coupling of the bare resonance, R, to the source. This coupling is characterized by a strength parameter, α^{R}. The second component, $\mathcal{B}_c$, signifies the direct transition from the source to the channel c. The formalism ensures that the complete production vector gets dressed via the final state interaction.

The $\mathcal{Q}$-*vector*, as discussed in Ref. [72, 79, 84], offers an alternative methodology for constructing a production amplitude:

$$\mathcal{A}_a(s) = \sum_c \mathcal{M}_{ac}(s) \mathcal{Q}_c(s)/n_c \,. \tag{50.42}$$

Here, $\mathcal{Q}_c(s)$ represents a smooth function of s and can be parameterized using a polynomial series. The unitarity condition of Eq. (50.19) is satisfied when $\mathcal{Q}_c(s)$ is a real function and in particular does not have singularities above the lowest threshold for all channels c. Besides these conditions $\mathcal{Q}_c(s)$ is arbitrary. In a study of $\gamma\gamma \to \pi\pi$, *cf.* Ref. [66, 67] a low-order polynomial is claimed to be sufficient to parameterize the energy dependence of the function $\mathcal{Q}_c(s)$. The $\mathcal{Q}$-vector method is convenient, if the full matrix $\mathcal{M}$ is known, *cf.* Ref. [79]. An important distinction between the $\mathcal{P}$-vector and the $\mathcal{Q}$-vector methods is highlighted in [83]. When the two-particle scattering amplitude approaches zero, the production amplitude in the $\mathcal{Q}$-vector construction unavoidably vanishes for finite values of $\mathcal{Q}_c$, whereas it remains non-zero in the $\mathcal{P}$-vector approach.

Traditionally, amplitudes constructed using the $\mathcal{K}$-matrix technique exclude the left-hand cuts. Nevertheless, these can be customarily incorporated into the function b_{ba} from Eq. (50.38) for the scattering amplitude [85, 86]. Similarly, for the production amplitude, the functions $\mathcal{B}_c$ and $\mathcal{Q}_c$ from Eq. (50.40) and Eq. (50.42), respectively, might also encompass the left-hand cuts. Those can often be parameterized by low order polynomials [66, 67, 87].

The position of the resonance poles can be determined by examining the zeros of the analytic function $\det[1 - \mathcal{K} \, i\rho \, n^2]$. Owing to the ρ factor, this determinant exhibits a complex multisheet structure. Nonetheless, the nearest unphysical sheet usually has the highest influence to the physical region. It is always the one which is determined by the heaviest threshold below the studied point in s (*cf.* Fig. 50.3). If for a given resonance the pole closest to the physical axis is not located on a sheet that connects directly to the physical axis, it is possible that $\mathcal{K}$-matrix fits do not allow one to fix the pole parameters, since a larger distance of the pole to the physical axis can be balanced by increased residues — for a detailed discussion see Ref. [88].

50.3.3 *Further improvements: Chew-Mandelstam function*

The $\mathcal{K}$-matrix framework often enables an accurate fit of physical amplitudes and is straightforward to handle. However, it does present a significant drawback: it breaches constraints imposed
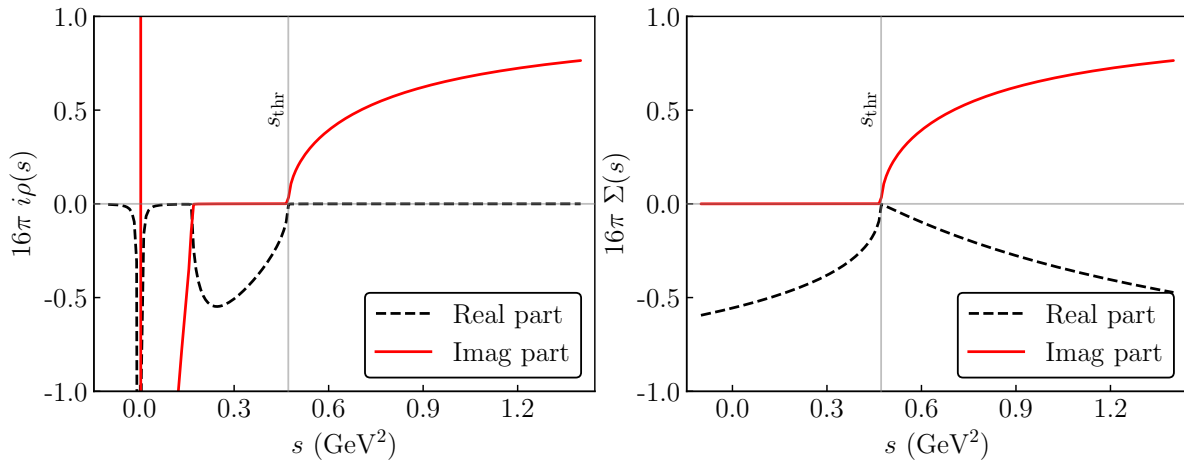
Figure 50.6: Comparison of the $i\rho$ function (left plot) to the *Chew-Mandelstam function* from Eq. (50.44) (right plot), evaluated for the case of S-wave $\eta\pi$ scattering. The values of s are taken slightly above the real axis, $s + i0$. The solid red line shows the imaginary part that is the same for both functions above threshold. The dashed black line presents the real part. One finds indications of the unphysical left-hand singularities of the function $i\rho$ on the left plot, while the Chew-Mandelstam function in analytic below the two-particle threshold.

by analyticity. For instance, ρ_a, as defined in Eq. (50.11), is not well-defined at $s = 0$. Moreover, in cases of unequal masses, it manifests an unphysical cut, as depicted in the left panel of Fig. 50.6.

A method to improve the analytic properties has been suggested in Refs. [89–93]. This approach replaces the term $i\rho_a(s)n_a^2$ from Eq. (50.37) with the analytic function $\Sigma_a(s)$, known as the Chew-Mandelstam function. This function produces the imaginary part $i\rho_a(s)n_a^2$ on the right-hand cut, while maintaining analyticity on the left-hand side, as represented by the once subtracted dispersion integral:

$$\Sigma_a(s + i0) = \frac{s - s_{\text{thr}_a}}{\pi} \int_{s_{\text{thr}_a}}^{\infty} \frac{\rho_a(s')n_a^2(s')}{(s' - s_{\text{thr}_a})(s' - s - i0)} \, ds'. \tag{50.43}$$

Here, we chose the channel threshold, s_{thr_a}, as the subtraction point, and assumed that the subtraction constant is absorbed into the other parameters used for the amplitude. For an S-wave where $n_a = 1$, the integral has a closed form [37, 91]:

$$\Sigma_a(s) = \frac{1}{16\pi^2}\left[\frac{2q_a}{\sqrt{s}}\log\frac{m_1^2 + m_2^2 - s + 2\sqrt{s}q_a}{2m_1 m_2} - (m_1^2 - m_2^2)\left(\frac{1}{s} - \frac{1}{(m_1 + m_2)^2}\right)\log\frac{m_1}{m_2}\right], \tag{50.44}$$

where m_1 and m_2 are masses of the final-state particles in channel a, with $s_{\text{thr}_a} = (m_1 + m_2)^2$. The function's behavior along the real axis is illustrated in the right panel of Fig. 50.6. A further discussion of the calculation of the Chew-Mandelstam function can be found in Refs. [94, 95].

If there is only a single resonance in a given channel, it is possible to feed the imaginary part of the Breit–Wigner function, Eq. (50.30) with an energy-dependent width, directly into a dispersion integral to get a resonance propagator with the correct analytic structure [96, 97].

50.3.4 *Effective-range expansion and scattering-length approximation*

For elastic scattering, $\eta_b = 1$, Eq. (50.14) simplifies to

$$f_{bb} = e^{i\delta}\sin(\delta) = \frac{q}{q\cot(\delta) - iq} \ , \tag{50.45}$$

where q is the relative momentum of the scattering particles. For S-waves one may then employ the *effective-range expansion* [98,99] (ERE)

$$q \cot \delta = \frac{1}{a} + \frac{1}{2}rq^2 + O(r^3 q^4) \, , \tag{50.46}$$

whose radius of convergence is set by the closest non-analyticity, which may be the next threshold, a left-hand cut or a zero in the amplitude which is equivalent to a pole in $q \cot \delta$. The ERE is understood to be an expansion in $R_f q$, where R_f denotes the range of forces provided by the inverse of the lightest exchange particle allowed. The *scattering length*, a, is then defined as the first term in an expansion of the real part of the inverse scattering amplitude. The sign convention used in Eq. (50.46) is the one commonly employed in particle physics. In this convention a positive scattering length indicates attraction; if, however, the attraction is strong enough to generate a bound state, the scattering length changes sign and turns negative. A negative scattering length also occurs for repulsive interactions. Note that in nuclear physics the leading term in the expansion of Eq. (50.46) is usually defined as $-1/a$ such that *e.g.* a bound state would be related to a positive scattering length. The parameter r is called the *effective range*. Especially in cases where the scattering length is large the ERE not only describes the low energy scattering well but also allows for an analytic continuation to find bound states below threshold by proper analytic continuation. This method was, *e.g.*, employed recently to analyze near threshold scattering phase shifts for $D^{*+} D^0$ scattering found in lattice analyses to extract properties of the $T_{cc}(3875)^+$ [100–102] at unphysical pion masses. It should be stressed that the analyses of the lattice data might call for a modification to account for the nearby left-hand cut which sets the radius of convergence of the ERE [103].

When considering only the scattering length within the ERE, the scattering amplitude is represented as:

$$\mathcal{M}(s) = \frac{8\pi\sqrt{s}}{1/a - iq(s)} \, . \tag{50.47}$$

The scattering length is thus proportional to the value of the amplitude at threshold. It is worth noting that the scattering length approximation is applicable only in a very limited energy range, however, might well be appropriate to analyze the recently discovered narrow near-threshold states [104,105]. Examples of such analyses can be found in Refs. [106–108]. Moreover, it is possible to introduce the effect of a weakly coupled lower channel [109,110]. Such coupling results in a positive imaginary part of the scattering length. It is also crucial to highlight that for large a values, the amplitude of Eq. (50.47) develops a near-threshold pole located on the physical or unphysical sheet for negative or positive values of a, respectively. For readers interested in a exploration of how close-to-threshold poles interact with remote thresholds, we refer to Ref. [111].

While easy to use, it is important to stress, however, that the approximation in Eq. (50.47) is a specific choice of the dynamic function. This choice results in a single pole close to the physical region, suggesting that the state under study has the characteristics of a hadronic molecule, as discussed in references such as [108, 112–114]. Virtual states are discussed in this context in Ref. [115].

50.3.5 *Two-potential decomposition*

Another advanced technique to construct the scattering amplitude, which is widely used in the literature [69, 116–121], is based on the two-potential formalism [122]. While it is possible to formulate this method for the full unprojected amplitude $\mathcal{M}_{ba}(s,t)$, for clarity, we focus on presenting the equations in their partial-wave-projected form.

The scattering amplitude, $\mathcal{M}(s)$, can be broken down into two components: a background part and a pole part. This can be represented as:

$$\mathcal{M}(s) = \mathcal{M}^{\mathrm{b.g.}}(s) + \mathcal{M}^{\mathrm{pole}}(s) \,. \tag{50.48}$$

It is important to note that the division presented in Eq. (50.48) is not unique and model-dependent. This is further discussed in references such as [123, 124]. The background scattering matrix is assumed to be unitary by itself. One approach to parameterize it, especially at lower energies, is by using phase shifts and inelasticities, as seen in [69, 120, 121]. Alternatively, it can be computed based on some potential, $V^{\mathrm{b.g.}}$, fed into a proper scattering equation [118, 119].

The complete amplitude, $\mathcal{M}$, from Eq. (50.48) is unitary, if the pole part follows a specific construction. Namely,

$$\mathcal{M}_{ab}^{\mathrm{pole}}(s) = \Omega_{ac}(s) \, [1 - V^{\mathrm{R}}(s)\Sigma^u(s)]_{cd}^{-1} V_{de}^{\mathrm{R}}(s) \, \Omega_{eb}^T(s) \,. \tag{50.49}$$

In this context, we introduce the vertex functions, denoted as $\Omega_{ab}(s)$, and the resonance potential, represented as $V^{\mathrm{R}}(s)$. This potential operates as a matrix in the channel space and can be expressed as:

$$V_{ab}^{\mathrm{R}}(s) = \sum_{\mathrm{R}} \frac{g_a^{\mathrm{R}} \, g_b^{\mathrm{R}}}{m_{\mathrm{R}}^2 - s} \,. \tag{50.50}$$

The term Σ_{ab}^u represents the self-energy matrix. Additionally, g_a^{R} denotes the bare coupling of the resonance, labeled as R, to the channel a, and m_{R} is its bare mass. The vertex functions obey a unitarity relation similar to the production amplitude in Eq. (50.8). However, in this case, the final state interaction is determined by $\mathcal{M}^{\mathrm{b.g.}}$. This can be represented as:

$$\mathrm{Disc}\, \Omega_{ab}(s) = 2i \sum_c \mathcal{M}_{ca}^{\mathrm{b.g.}\,*}(s) \, \rho_c(s) \, \Omega_{cb}(s) \,. \tag{50.51}$$

When using low-energy phase shifts for the background term, it is practical to express the vertex functions in terms of an Omnès matrix, as discussed in [121]. The matrix reduces to the well-known Omnès function

$$\Omega(s) = \exp \left(\frac{s}{\pi} \int_{s_{\mathrm{thr}}}^{\infty} \mathrm{d}s' \frac{\delta^{\mathrm{b.g.}}(s')}{s'(s' - s - i\epsilon)} \right) \tag{50.52}$$

in the single-channel case [125], where $\delta^{\mathrm{b.g.}}(s)$ denotes the phase of the background scattering matrix $\mathcal{M}^{\mathrm{b.g.}}(s)$. The discontinuity associated with the self-energy matrix, $\Sigma^u(s)$, is given by:

$$\mathrm{Disc}\, \Sigma_{ab}^u(s) = 2i \sum_c \Omega_{ca}^*(s) \, \rho_c(s) \, \Omega_{cb}(s) \,. \tag{50.53}$$

To determine the real part of Σ^u, one can use Eq. (50.53) with a properly subtracted dispersion integral — *cf.* Eq. (50.43).

When $\mathcal{M}^{\mathrm{b.g.}}$ is unitary, the full amplitude is unitary given Eq. (50.49). However, it is essential to note that the pole term alone is not unitary unless the background amplitude vanishes. Under such conditions, the described amplitude simplifies to the the $\mathcal{K}$-matrix construction with improved analytic behavior as detained in Sec. 50.3.3. Neglecting non-pole terms is not a good approximation for certain interactions, such as the scalar-isoscalar $\pi\pi$ at low energies, as discussed in [126]. However, for higher partial waves, this approximation is generally effective.

A production amplitude consistent with Eq. (50.49) reads [120, 121]:

$$\mathcal{A}_a^{\mathrm{pole}}(s) = \Omega_{ac}(s) \, [1 - V^{\mathrm{R}}(s)\Sigma^u(s)]_{cd}^{-1} \mathcal{P}_d \,, \tag{50.54}$$

with function $\mathcal{P}_d$ given in Eq. (50.40). This form was employed in Refs. [120, 121] to treat the pion vector and scalar form factor, respectively, and in Ref. [69] for the scalar πK form factor.

There has been considerable interest in the $3 \to 3$ scattering recently, particularly in light of new data on three-hadron interaction [127] and advancements in lattice calculations [128]. One finds that the methodologies devised for accounting for one-pion exchange bear a resemblance to the two-potential decomposition. For details see Ref. [129], also Eq. (93) in Ref. [130].

References

[1] M. Albaladejo *et al.* (JPAC), Prog. Part. Nucl. Phys. **127**, 103981 (2022), [arXiv:2112.13436].

[2] M. Mai, U.-G. Meißner and C. Urbach, Phys. Rept. **1001**, 1 (2023), [arXiv:2206.01477].

[3] M. Jacob and G. C. Wick, Annals Phys. **7**, 404 (1959), [Annals Phys.281,774(2000)].

[4] C. Zemach, Phys. Rev. **140B**, 97, 109 (1965).

[5] A. V. Anisovich *et al.*, J. Phys. **G28**, 15 (2002), [hep-ph/0105330].

[6] M. E. Peskin and D. V. Schroeder, *An Introduction to quantum field theory*, Addison-Wesley, Reading, USA (1995), ISBN 978-0-201-50397-5.

[7] V. N. Gribov, Y. L. Dokshitzer and J. Nyiri, *Strong Interactions of Hadrons at High Energies – Gribov Lectures on Theoretical Physics*, Cambridge University Press, Cambridge (2009).

[8] M. Doring *et al.*, Nucl. Phys. A **829**, 170 (2009), [arXiv:0903.4337].

[9] L. Landau, Nucl. Phys. **13**, 181 (1959).

[10] R. Cutkosky, J. Math. Phys. **1**, 429 (1960).

[11] M. Kato, Annals Phys. **31**, 1, 130 (1965).

[12] A. M. Badalian *et al.*, Phys. Rept. **82**, 31 (1982).

[13] V. Baru *et al.*, Phys. Rev. D **99**, 9, 094013 (2019), [arXiv:1901.10319].

[14] G. Calucci, L. Fonda and G. C. Ghirardi, Phys. Rev. **166**, 1719 (1968).

[15] S. Coleman and R. E. Norton, Nuovo Cim. **38**, 438 (1965).

[16] C. Schmid, Phys. Rev. **154**, 5, 1363 (1967).

[17] I. J. R. Aitchison and C. Kacser, Nuovo Cim. A **40**, 2, 576 (1965).

[18] M. Mikhasenko, B. Ketzer and A. Sarantsev, Phys. Rev. D **91**, 9, 094015 (2015), [arXiv:1501.07023].

[19] M. Bayar *et al.*, Phys. Rev. **D94**, 7, 074039 (2016), [arXiv:1609.04133].

[20] F. Aceti, L. R. Dai and E. Oset, Phys. Rev. **D94**, 9, 096015 (2016), [arXiv:1606.06893].

[21] J.-J. Wu *et al.*, Phys. Rev. Lett. **108**, 081803 (2012), [arXiv:1108.3772].

[22] L. D. Roper, Phys. Rev. Lett. **12**, 340 (1964).

[23] J. R. Pelaez, Phys. Rept. **658**, 1 (2016), [arXiv:1510.00653].

[24] R. Omnès, *Introduction to Particle Physics*, Frontiers in physics, Wiley-Interscience (1971), ISBN 9780471653721.

[25] R. Omnès and M. Froissart, *Mandelstam Theory and Regge Poles: An Introduction for Experimentalists*, Frontiers in physics, W.A. Benjamin (1963), URL https://books.google.fr/books?id=O8pEAAAAIAAJ.

[26] M. Fukugita and K. Igi, Phys. Rept. **31**, 237 (1977).

[27] S. Weinberg, *The Quantum theory of fields. Vol. 1: Foundations*, Cambridge University Press (2005), ISBN 978-0-521-67053-1, 978-0-511-25204-4.

[28] S. M. Roy, Phys. Lett. **36B**, 353 (1971).

[29] B. Ananthanarayan *et al.*, Phys. Rept. **353**, 207 (2001), [hep-ph/0005297].

[30] G. Colangelo, J. Gasser and H. Leutwyler, Nucl. Phys. **B603**, 125 (2001), [hep-ph/0103088].

[31] R. Garcia-Martin *et al.*, Phys. Rev. D **83**, 074004 (2011), [arXiv:1102.2183].

[32] P. Buettiker, S. Descotes-Genon and B. Moussallam, Eur. Phys. J. **C33**, 409 (2004), [hep-ph/0310283].

[33] M. Hoferichter, D. R. Phillips and C. Schat, Eur. Phys. J. **C71**, 1743 (2011), [arXiv:1106.4147].

[34] G. E. Hite and F. Steiner, Nuovo Cim. A **18**, 237 (1973).

[35] M. Hoferichter *et al.*, Phys. Rept. **625**, 1 (2016), [arXiv:1510.06039].

[36] D. I. Olive, Il Nuovo Cimento (1955-1965) **73**, 1, 73 (1962), ISSN 1827-6121, URL https://doi.org/10.1007/BF02754344.

[37] J. L. Basdevant and E. L. Berger, Phys. Rev. **D16**, 657 (1977).

[38] N. N. Khuri and S. B. Treiman, Phys. Rev. **119**, 1115 (1960).

[39] I. J. R. Aitchison and R. Pasquier, Phys. Rev. **152**, 4, 1274 (1966).

[40] J. Kambor, C. Wiesendanger and D. Wyler, Nucl. Phys. B **465**, 215 (1996), [hep-ph/9509374].

[41] A. V. Anisovich and H. Leutwyler, Phys. Lett. B **375**, 335 (1996), [hep-ph/9601237].

[42] P. Guo *et al.*, Phys. Lett. **B771**, 497 (2017), [arXiv:1608.01447].

[43] M. Albaladejo and B. Moussallam, Eur. Phys. J. **C77**, 8, 508 (2017), [arXiv:1702.04931].

[44] G. Colangelo *et al.*, Eur. Phys. J. **C78**, 11, 947 (2018), [arXiv:1807.11937].

[45] K. Kampf *et al.*, Phys. Rev. D **101**, 7, 074043 (2020), [arXiv:1911.11762].

[46] T. Isken *et al.*, Eur. Phys. J. **C77**, 7, 489 (2017), [arXiv:1705.04339].

[47] F. Niecknig, B. Kubis and S. P. Schneider, Eur. Phys. J. **C72**, 2014 (2012), [arXiv:1203.2501].

[48] I. V. Danilkin *et al.*, Phys. Rev. **D91**, 9, 094029 (2015), [arXiv:1409.7708].

[49] M. Dax, T. Isken and B. Kubis, Eur. Phys. J. C **78**, 10, 859 (2018), [arXiv:1808.08957].

[50] M. Albaladejo *et al.* (JPAC), Eur. Phys. J. C **80**, 12, 1107 (2020), [arXiv:2006.01058].

[51] M. Albaladejo *et al.* (JPAC), Phys. Rev. D **101**, 5, 054018 (2020), [arXiv:1910.03107].

[52] D. Stamen *et al.*, Eur. Phys. J. C **83**, 6, 510 (2023), [Erratum: Eur.Phys.J.C 83, 586 (2023)], [arXiv:2212.11767].

[53] F. Niecknig and B. Kubis, JHEP **10**, 142 (2015), [arXiv:1509.03188].

[54] F. Niecknig and B. Kubis, Phys. Lett. **B780**, 471 (2018), [arXiv:1708.00446].

[55] M. Albaladejo *et al.* (JPAC), Phys. Rev. D **108**, 1, 014035 (2023), [arXiv:2304.09736].

[56] M. Mikhasenko *et al.* (JPAC), Phys. Rev. D **101**, 3, 034033 (2020), [arXiv:1910.04566].

[57] K. M. Watson, Phys. Rev. **95**, 228 (1954).

[58] S. Willenbrock (2022), [arXiv:2203.11056].

[59] Z.-Q. Wang *et al.*, Phys. Rev. D **105**, 7, 074016 (2022), [arXiv:2201.00492].

[60] V. Burkert *et al.*, Phys. Lett. B **844**, 138070 (2023), [arXiv:2207.08472].

[61] M. Aghasyan *et al.* (COMPASS), Phys. Rev. D **98**, 9, 092003 (2018), [arXiv:1802.05913].

[62] R. Aaij *et al.* (LHCb), Phys. Rev. D **94**, 7, 072001 (2016), [arXiv:1608.01289].

[63] R. Aaij *et al.* (LHCb), Phys. Rev. D **92**, 1, 012012 (2015), [arXiv:1505.01505].

[64] R. Aaij *et al.* (LHCb), Phys. Rev. D **91**, 9, 092002 (2015), [Erratum: Phys.Rev.D 93, 119901 (2016)], [arXiv:1503.02995].

[65] R. Aaij *et al.* (LHCb), Phys. Rev. D **102**, 112003 (2020), [arXiv:2009.00026].

[66] D. Morgan and M. R. Pennington, Z. Phys. **C37**, 431 (1988), [Erratum: Z. Phys.C39,590(1988)].

[67] D. Morgan and M. R. Pennington, Z. Phys. **C48**, 623 (1990).

[68] B. Moussallam, Eur. Phys. J. C **71**, 1814 (2011), [arXiv:1110.6074].

[69] L. Von Detten *et al.*, Eur. Phys. J. C **81**, 5, 420 (2021), [arXiv:2103.01966].

[70] J. M. Blatt and V. F. Weisskopf, *Theoretical nuclear physics*, Springer, New York (1952), ISBN 9780471080190.

[71] F. Von Hippel and C. Quigg, Phys. Rev. **D5**, 624 (1972).

[72] S. U. Chung *et al.*, Annalen Phys. **4**, 404 (1995).

[73] S. M. Flatte, Phys. Lett. **63B**, 224 (1976).

[74] V. V. Anisovich and A. V. Sarantsev, Eur. Phys. J. **A16**, 229 (2003), [hep-ph/0204328].

[75] V. Baru *et al.*, Eur. Phys. J. **A23**, 523 (2005), [arXiv:nucl-th/0410099].

[76] R. Aaij *et al.* (LHCb), Phys. Rev. D **108**, 1, L011103 (2023), [arXiv:2204.12597].

[77] J. P. Lees *et al.* (BaBar), Phys. Rev. D **86**, 032013 (2012), [arXiv:1205.2228].

[78] I. J. R. Aitchison, Nucl. Phys. **A189**, 417 (1972).

[79] K. L. Au, D. Morgan and M. R. Pennington, Phys. Rev. D **35**, 1633 (1987).

[80] J. J. Dudek, R. G. Edwards and D. J. Wilson (Hadron Spectrum), Phys. Rev. **D93**, 9, 094506 (2016), [arXiv:1602.05122].

[81] R. A. Briceno *et al.*, Phys. Rev. **D97**, 5, 054513 (2018), [arXiv:1708.06667].

[82] A. J. Woss *et al.*, Phys. Rev. D **100**, 5, 054506 (2019), [arXiv:1904.04136].

[83] I. J. R. Aitchison (2015), [arXiv:1507.02697].

[84] R. N. Cahn and P. V. Landshoff, Nucl. Phys. **B266**, 451 (1986).

[85] J. R. Pelaez, A. Rodas and J. Ruiz De Elvira, Eur. Phys. J. C **79**, 12, 1008 (2019), [arXiv:1907.13162].

[86] I. Danilkin *et al.*, Phys. Rev. D **107**, 7, 074021 (2023), [arXiv:2206.15223].

[87] B. Kubis and J. Plenter, Eur. Phys. J. C **75**, 6, 283 (2015), [arXiv:1504.02588].

[88] A. Asokan *et al.* (2022), [arXiv:2212.07856].

[89] G. J. Gounaris and J. J. Sakurai, Phys. Rev. Lett. **21**, 244 (1968).

[90] M. R. Pennington *et al.*, Eur. Phys. J. **C56**, 1 (2008), [arXiv:0803.3389].

[91] J. A. Oller and E. Oset, Phys. Rev. **D60**, 074023 (1999), [hep-ph/9809337].

[92] N. N. Achasov and A. V. Kiselev, Phys. Rev. **D83**, 054008 (2011), [arXiv:1011.4446].

[93] A. V. Anisovich *et al.*, Phys. Rev. **D84**, 076001 (2011).

[94] J. H. Reid and N. N. Trofimenkoff, J. Math. Phys. **25**, 3540 (1984).

[95] J. A. Oller and U. G. Meissner, Phys. Lett. B **500**, 263 (2001), [hep-ph/0011146].

[96] E. L. Lomon and S. Pacetti, Phys. Rev. **D85**, 113004 (2012), [Erratum: Phys. Rev.D86,039901(2012)], [arXiv:1201.6126].

[97] B. Moussallam, Eur. Phys. J. **C73**, 2539 (2013), [arXiv:1305.3143].

[98] J. M. Blatt and J. D. Jackson, Phys. Rev. **76**, 18 (1949).

[99] H. A. Bethe, Phys. Rev. **76**, 38 (1949).

[100] M. Padmanath and S. Prelovsek, Phys. Rev. Lett. **129**, 3, 032002 (2022), [arXiv:2202.10110].

[101] S. Chen *et al.*, Phys. Lett. B **833**, 137391 (2022), [arXiv:2206.06185].

[102] Y. Lyu *et al.* (2023), [arXiv:2302.04505].

[103] M.-L. Du *et al.*, Phys. Rev. Lett. **131**, 13, 131903 (2023), [arXiv:2303.09441].

[104] S. K. Choi *et al.* (Belle), Phys. Rev. Lett. **91**, 262001 (2003), [hep-ex/0309032].

[105] R. Aaij *et al.* (LHCb), Phys. Rev. Lett. **122**, 22, 222001 (2019), [arXiv:1904.03947].

[106] E. Braaten and J. Stapleton, Phys. Rev. D **81**, 014019 (2010), [arXiv:0907.3167].

[107] V. Baru *et al.*, Eur. Phys. J. **A44**, 93 (2010), [arXiv:1001.0369].

[108] C. Fernández-Ramírez *et al.* (JPAC), Phys. Rev. Lett. **123**, 9, 092001 (2019), [arXiv:1904.10021].

[109] C. Hanhart *et al.*, Phys. Rev. Lett. **115**, 20, 202001 (2015), [arXiv:1507.00382].

[110] F. K. Guo *et al.*, Phys. Rev. D **93**, 7, 074031 (2016), [arXiv:1602.00940].

[111] X.-K. Dong, F.-K. Guo and B.-S. Zou, Phys. Rev. Lett. **126**, 15, 152001 (2021), [arXiv:2011.14517].

[112] D. Morgan, Nucl. Phys. **A543**, 632 (1992).

[113] V. Baru *et al.*, Phys. Lett. **B586**, 53 (2004), [hep-ph/0308129].

[114] F.-K. Guo *et al.*, Rev. Mod. Phys. **90**, 1, 015004 (2018), [arXiv:1705.00141].

[115] I. Matuschek *et al.*, Eur. Phys. J. A **57**, 3, 101 (2021), [arXiv:2007.05329].

[116] I. R. Afnan and B. Blankleider, Phys. Rev. **C22**, 1638 (1980).

[117] A. D. Lahiff and I. R. Afnan, Phys. Rev. **C60**, 024608 (1999), [arXiv:nucl-th/9903058].

[118] A. Matsuyama, T. Sato and T. S. H. Lee, Phys. Rept. **439**, 193 (2007), [arXiv:nucl-th/0608051].

[119] D. Ronchen *et al.*, Eur. Phys. J. **A49**, 44 (2013), [arXiv:1211.6998].

[120] C. Hanhart, Phys. Lett. **B715**, 170 (2012), [arXiv:1203.6839].

[121] S. Ropertz, C. Hanhart and B. Kubis, Eur. Phys. J. **C78**, 12, 1000 (2018), [arXiv:1809.06867].

[122] K. Nakano, Phys. Rev. **C26**, 1123 (1982).

[123] D. Djukanovic, J. Gegelia and S. Scherer, Phys. Rev. **D76**, 037501 (2007), [arXiv:0707.2030].

[124] M. Doring *et al.*, Phys. Lett. **B681**, 26 (2009), [arXiv:0903.1781].

[125] R. Omnes, Nuovo Cim. **8**, 316 (1958).

[126] J. Gasser and U. G. Meissner, Nucl. Phys. **B357**, 90 (1991).

[127] B. Ketzer, B. Grube and D. Ryabchikov, Prog. Part. Nucl. Phys. **113**, 103755 (2020), [arXiv:1909.06366].

[128] B. Hörz and A. Hanlon, Phys. Rev. Lett. **123**, 14, 142002 (2019), [arXiv:1905.04277].

[129] M. Mikhasenko *et al.*, JHEP **08**, 080 (2019), [arXiv:1904.11894].

[130] M. T. Hansen and S. R. Sharpe, Phys. Rev. D **92**, 11, 114509 (2015), [arXiv:1504.04248].